

Electric field-induced second-order nonlinear optical effects in silicon waveguides

E. Timurdogan*, C. V. Poulton, M. J. Byrd and M. R. Watts

The symmetry of crystalline silicon inhibits a second-order optical nonlinear susceptibility, $\chi^{(2)}$, in complementary metal-oxide-semiconductor-compatible silicon photonic platforms. However, $\chi^{(2)}$ is required for important processes such as phase-only modulation, second-harmonic generation (SHG) and sum/difference frequency generation. Here, we break the crystalline symmetry by applying direct-current fields across p-i-n junctions in silicon ridge waveguides and induce a $\chi^{(2)}$ proportional to the large $\chi^{(3)}$ of silicon. The obtained $\chi^{(2)}$ is first used to perturb the permittivity (the direct-current Kerr effect) and achieve phase-only modulation. Second, the spatial distribution of $\chi^{(2)}$ is altered by periodically patterning p-i-n junctions to quasi-phase-match pump and second-harmonic modes and realize SHG. We measure a maximum SHG efficiency of $P_{2\omega}/P_{\omega}^2 = 13 \pm 0.5\% \text{ W}^{-1}$ at $\lambda_{\omega} = 2.29 \mu\text{m}$ and with field-induced $\chi^{(2)} = 41 \pm 1.5 \text{ pm V}^{-1}$. We expect such field-induced $\chi^{(2)}$ in silicon to lead to a new class of complex integrated devices such as carrier-envelope offset frequency stabilizers, terahertz generators, optical parametric oscillators and chirp-free modulators.

Second-order nonlinear optical effects are close to zero in complementary metal-oxide-semiconductor (CMOS)-compatible materials (for example, Si, SiN, SiO₂ and Ge), as these materials are centro-symmetric and the second-order nonlinear susceptibility $\chi^{(2)}$ is inhibited in the electric-dipole approximation¹. This provides a significant challenge for second-order nonlinear processes such as second-harmonic generation (SHG) and phase-only modulation in a CMOS-compatible platform. Due to this limitation, wavelength generation in silicon has been focused on third-harmonic generation^{2,3} and four-wave mixing^{4,5} using the third-order nonlinear susceptibility $\chi^{(3)}$ (ref. 6). Nonetheless, high-efficiency SHG is still required for common carrier-envelope frequency offset locking techniques⁷ and mid-infrared to telecom wavelength conversion.

Recently, $\chi^{(2)}$ in silicon has been realized thanks to a deposited SiN stressor layer that broke the centro-symmetry⁸. However, a low SHG efficiency of $P_{2\omega}/P_{\omega}^2 \approx 10^{-5}\% \text{ W}^{-1}$ was measured due to the phase mismatch between the pump and signal wavelengths. SHG in SiN waveguides^{9,10} has also been achieved, but again with a low SHG efficiency of $P_{2\omega}/P_{\omega}^2 = 0.1\% \text{ W}^{-1}$ (ref. 10). These efficiencies are indeed low compared to SHG with non-centro-symmetric media characterized by large $\chi^{(2)}$, high modal overlap and phase matching between the pump and signal modes^{11–13}. To the best of our own knowledge, these features have not been shown simultaneously on a CMOS-compatible platform.

An asymmetry is introduced into the crystalline structure of a material in the presence of an applied electric field because the dipole moments orient themselves in the direction of the applied field^{14,15}. Through this process, the third-order nonlinear susceptibility $\chi^{(3)}$ is converted to $\chi^{(2)}$, enabling SHG and many other processes. This electric-field-induced SHG (EFISHG) was initially used for material parameter extraction from semiconductors¹⁴ and field measurements of silicon metal-oxide-semiconductor (MOS) transistor interfaces¹⁵. This process was also achieved using nonlinear polymers within silicon slot waveguides^{16,17}. Recently, a weak field-induced SHG contribution was reported as part of the SHG in strained silicon waveguides due to positive charges in the silicon interfaces¹⁸. A field-induced $\chi^{(2)}$ can be strong in silicon because it exhibits a large $\chi^{(3)}$ (ref. 19); in fact, field-induced nonlinear optical effects based on high-order susceptibilities scale with the applied electric field^{1,15}, and the upper

limit of the field-induced $\chi^{(2)}$ is imposed by the breakdown field of silicon ($E_{\text{dc}}^x \approx 40 \text{ V } \mu\text{m}^{-1}$) (ref. 20). However, phase matching is challenging for many optical wavelengths in silicon waveguides, and these wavelengths can instead be quasi-phase-matched with a periodically generated electric field²¹.

The field-induced $\chi^{(2)}$ can also perturb the electric permittivity and introduce a phase shift. This is referred to as the d.c. Kerr effect or quadratic electro-optic Kerr effect^{19,22}; this is an inherently phase-matched process. So far, high-speed phase shifting in silicon has been achieved with the plasma-dispersion effect²⁰, as the absence of $\chi^{(2)}$ prevents the realization of the Pockels effect commonly used in LiNbO₃, for example. The drawback of the plasma-dispersion effect is that both real and imaginary parts of the refractive index are perturbed, which in turn introduces an amplitude chirp to the phase shift. By contrast, a field-induced $\chi^{(2)}$ can produce high-speed, phase-only shifts in silicon waveguides.

Here, we demonstrate the d.c. Kerr effect and EFISHG in integrated silicon ridge waveguides. We implanted the waveguides with ions to form compact p-i-n junctions, which concentrate electric fields and take advantage of the large $\chi^{(3)}$ of silicon. The d.c. Kerr effect was demonstrated in a silicon Mach-Zehnder interferometer (MZI) with a voltage required to induce π phase shift for a given length ($V_{\pi}L$) of 2.8 V cm. For efficient EFISHG in silicon, the fundamental pump and signal modes are quasi-phase-matched with periodically patterned p-i-n junctions. In this configuration, a SHG efficiency of $P_{2\omega}/P_{\omega}^2 = 13 \pm 0.5\% \text{ W}^{-1}$ at $\lambda_{\omega} = 2\lambda_{2\omega} = 2.29 \mu\text{m}$ was measured, the most efficient CMOS-compatible SHG to date. This corresponds to an effective field-induced $\bar{\chi}^{(2)}$ of $41 \pm 1.5 \text{ pm V}^{-1}$ at an applied d.c. bias of -21 V. Varying the waveguide width and the spatial period, we recorded SHG at multiple wavelengths spanning from $\lambda_{\omega} = 2.16 \mu\text{m}$ to 2.42 μm . Furthermore, the signal power scaled quadratically with pump power and proportionally with the applied reverse bias, confirming the nonlinear origin of the EFISHG. The SHG spectrum follows a sinc²-like envelope, in good agreement with theory.

Field-induced $\chi^{(2)}$ theory

The d.c. Kerr effect and EFISHG are effective $\chi^{(2)}$ processes that can be derived from a material exhibiting $\chi^{(3)}$. The d.c. Kerr effect is an

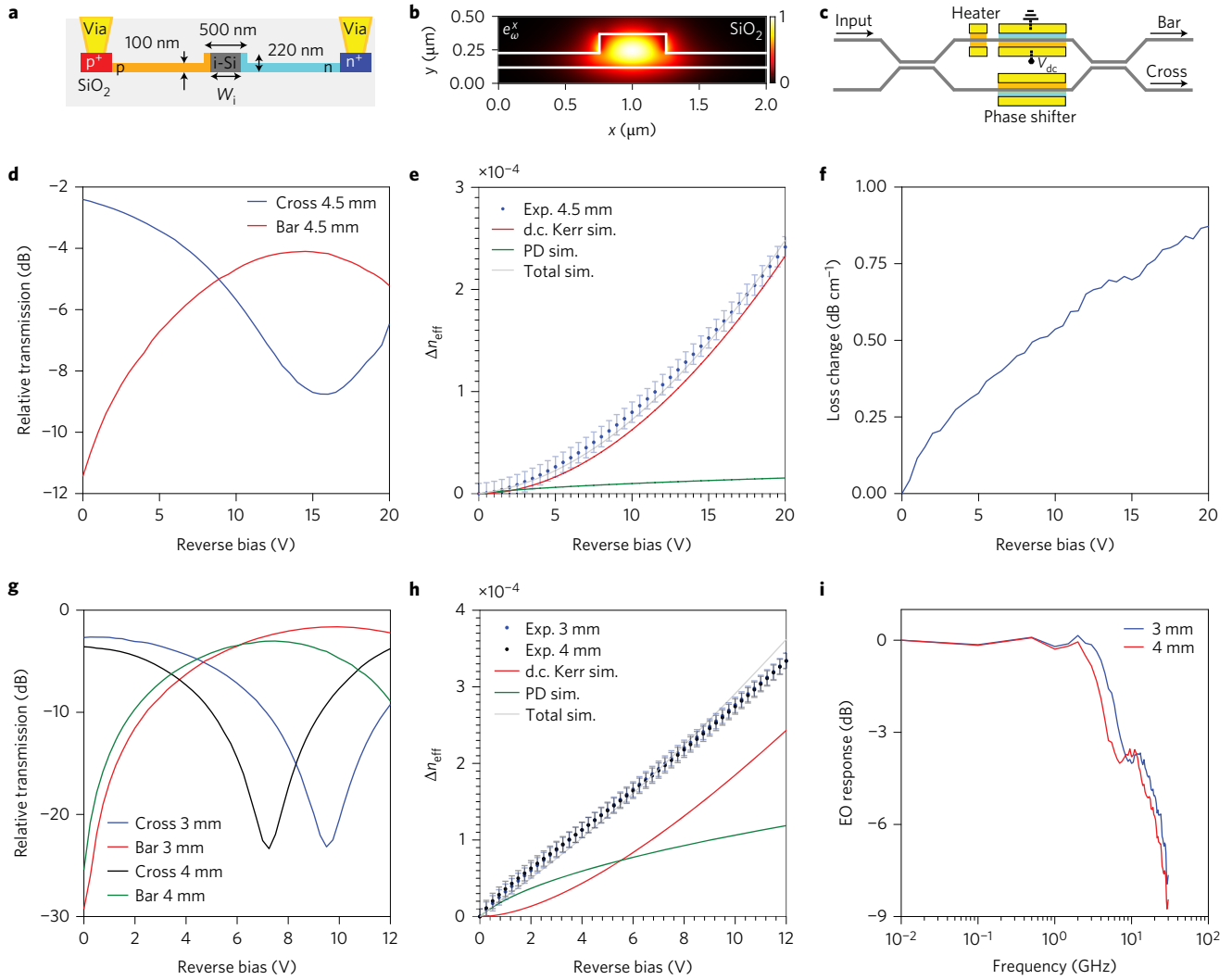


Figure 1 | The d.c. Kerr effect in silicon. **a**, Important device dimensions of the d.c. Kerr silicon ridge waveguide with p-i-n junction. **b**, Normalized fundamental TE modal electric-field profile (e_{ω}^x) of the structure. **c**, Mach-Zehnder interferometer (MZI) configuration with two d.c. phase shifters and heater. **d**, Measured transmission spectra of the MZI ports with an intrinsic region $W_{i,1}$ and 4.5 mm phase shifter length. **e**, Measured refractive index perturbation for the phase shifter with intrinsic region $W_{i,1}$. Simulated d.c. Kerr, plasma-dispersion (PD) and total index perturbations are overlaid. **f**, Loss change of the phase shifter with intrinsic region $W_{i,1}$. **g**, Measured transmission spectra of the MZIs with intrinsic region $W_{i,2}$. **h**, Measured refractive index perturbations for phase shifters with intrinsic region $W_{i,2}$. Simulated data are overlaid. In **e, h**, the error bars represent inaccuracies and experimental errors determined by fibre-to-chip coupling. **i**, Electro-optic (EO) frequency response of the MZIs with intrinsic region $W_{i,2}$.

inherently phase-matched four-wave mixing process, involving two fundamental fields (e_{ω}) and two d.c. fields (E_{dc}) in the form of $\chi_{ijkl}^{(3)}(-\omega; \omega, 0, 0)$ (ref. 19). EFISHG is a four-wave mixing process that involves two pump fields (e_{ω}), an output harmonic signal field ($e_{2\omega}$) and a d.c. field (E_{dc}) in the form of $\chi_{ijkl}^{(3)}(-2\omega; \omega, \omega, 0)$ (ref. 19). For an applied d.c. field and optical fields along the x direction (E_{dc}^x and e_{ω}^x), the nonlinear displacement current of interest for isotropic silicon^{1,19} is

$$D = \varepsilon_0 \left[\underbrace{\varepsilon_{Si} e_{\omega}^x \cos(\omega t)}_{\text{Linear polarization}} + \underbrace{12 \chi_{xxxx}^{(3)} E_{dc}^x e_{\omega}^x \cos(\omega t)}_{\text{Electro-optic d.c. Kerr effect}} \right] + \underbrace{3 \chi_{xxxx}^{(3)} E_{dc}^x e_{\omega}^x \cos(2\omega t)}_{\text{Field-induced second harmonic (EFISHG)}} \quad (1)$$

where ε_0 and ε_{Si} are the vacuum and relative silicon permittivities, respectively. The EFISHG and d.c. Kerr effects induce a relative

permittivity related to the $\chi_{xxxx}^{(3)}$ tensor element and to the applied d.c. field. Both effects are present within the silicon transparency window. However, the EFISHG generated wavelength should also be within the window for high SHG efficiency.

Direct-current Kerr effect design

We first designed devices to demonstrate the d.c. Kerr effect and confirm a field-induced $\chi^{(2)}$, because phase-matching is inherently satisfied. We thus fabricated two silicon ridge waveguides with embedded p-i-n junctions (Fig. 1a). The core of the silicon waveguides has a width of 500 nm, with intrinsic region widths $W_{i,1}$ and $W_{i,2}$. The intrinsic regions were simulated using a process and device simulator (see Methods, ‘Process and electrical simulations’), fitting to $W_{i,1} = 500 + 2\sqrt{V_{dc} + 0.5}$ and $W_{i,2} = 200 + 58\sqrt{V_{dc} + 0.5}$ (in nm). The large intrinsic regions were chosen to observe a relatively large d.c. Kerr effect and minimize the relative electro-refractive permittivity change due to the plasma-dispersion effect²⁰. The fundamental transverse electric (TE) mode was selected for maximal confinement, and propagation

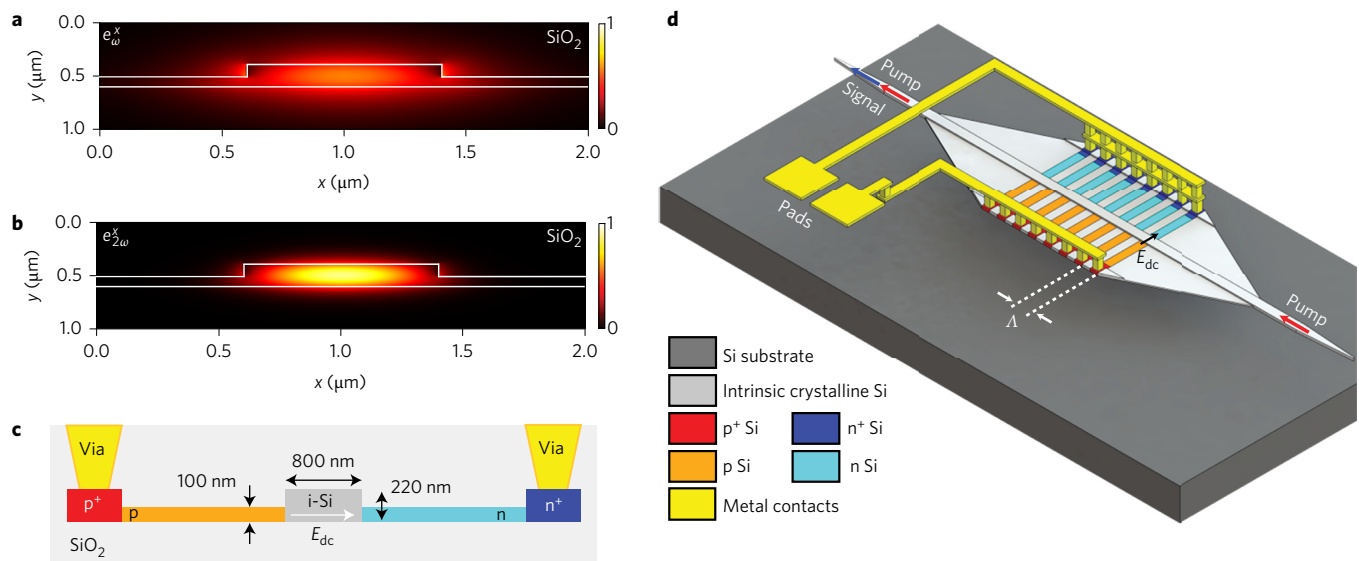


Figure 2 | Design of a field-induced second-harmonic generator. **a, b**, Normalized modal electric field profiles (e_{ω}^x , $e_{2\omega}^x$) at pump and second-harmonic signal wavelengths, showing maximal confinement inside the silicon core and a large overlap. **c**, Important device dimensions of the EFISHG device with p-i-n junction inside the silicon ridge waveguide. **d**, Three-dimensional sketch of the EFISHG device with silicon ridge waveguide and quasi-phase-matched spatially periodic patterning of the p-i-n junction. Dimensions are not to scale.

was chosen to be in the z direction. The optical mode profile e_{ω}^x (Fig. 1b) was simulated using a finite-difference mode solver²³. The x , y and z directions are aligned with the (0 1 0), (0 0 1) and (1 0 0) crystalline axes of the silicon wafer. The generated electric field in the p-i-n junction is aligned with the x direction (that is, $E_{dc}^z = E_{dc}^y = 0$) to utilize the diagonal (that is, the largest) tensor elements in the third-order nonlinear susceptibility of silicon, $\chi_{xxxx}^{(3)} = 2.45 \times 10^{-19} \text{ m}^2 \text{ V}^{-2}$ at $\lambda \approx 1.55 \mu\text{m}$ (ref. 4). The d.c. Kerr index perturbations for both intrinsic regions were simulated as a function of bias voltage, as shown in Fig. 1e,h (see Methods, ‘Eigenmode simulations’). Because the intrinsic silicon width changes slightly with applied voltage, the plasma-dispersion effect was also simulated using the method in ref. 24.

Direct-current Kerr effect results and discussion

We placed the designed silicon ridge waveguides in MZIs as optical phase shifters for characterizing the d.c. Kerr relative permittivity (Fig. 1c). MZIs with a 4.5-mm-long phase shifter with $W_{i,1}$ and 3- to 4-mm-long phase shifters with $W_{i,2}$ were fabricated on a 300-mm-diameter silicon-on-insulator (SOI) wafer (see Methods, ‘Device fabrication’). We recorded the optical power in the bar and cross ports of the MZIs as a function of applied voltage to a single arm of the MZIs (Fig. 1d,g), finding $V_{\pi}L$ values of 6.8 V cm and 2.8 V cm at $\lambda \approx 1.58 \mu\text{m}$ for intrinsic regions $W_{i,1}$ and $W_{i,2}$, respectively (see Methods, ‘Direct-current Kerr measurements’). The power difference between the cross and bar ports was normalized and fitted with $\cos(2\pi\Delta n(V_{dc})L/\lambda)$, where L is the Mach-Zehnder arm length and $\Delta n(V_{dc})$ is the induced refractive index as a function of applied voltage (Fig. 1e,h). The $\Delta n(V_{dc})$ was accurate to $\pm 10^{-5}$ due to curve-fitting inaccuracies and experimental errors determined by non-ideal fibre-to-chip coupling.

The observed relationship between refractive index change and voltage was quadratic and pseudolinear for intrinsic region widths $W_{i,1}$ and $W_{i,2}$, respectively. In these waveguides, the plasma-dispersion effect is expected to be small given the large intrinsic regions. Furthermore, we expect the plasma-dispersion effect to follow a dependence close to the square root of the applied voltage in light of the voltage dependence of the intrinsic region width. However, this is not observed due to the contribution from the d.c. Kerr effect. The plasma-dispersion effect in the waveguide

with an intrinsic region width of $W_{i,2}$ contributed to the change in refractive index two times less than the d.c. Kerr effect for large electric fields, and is negligible in the waveguide with the larger intrinsic region of width $W_{i,1}$. The loss change over 20 V was measured to be $0.9 \pm 0.2 \text{ dB cm}^{-1}$ for a straight waveguide (Fig. 1f), indicating minimal amplitude chirp. The uncertainty in the loss change was determined by imperfect repeatability of the fibre-to-chip coupling. In addition, we measured the MZI bandwidths of $W_{i,2}$ to ensure that the origin of the phase shift was not related to free carriers and carrier lifetimes, as is the case in refs 25 and 26. An a.c.-coupled small signal was applied through a 50 Ω terminated probe to the MZIs at the quadrature point, and the electro-optic response followed an expected RC-limited bandwidth (5 and 6.5 GHz for 4 and 3 mm phase shifters, respectively), as shown in Fig. 1i, which was higher than the carrier lifetimes reported in refs 25 and 26.

There are several potential advantages of d.c. Kerr-effect-based silicon phase shifters over plasma-dispersion-effect-based phase shifters. The waveguide core of a plasma-dispersion-effect-based phase shifter is doped, which results in an inherent insertion loss. Furthermore, the plasma-dispersion effect introduces a fundamental amplitude chirp due to perturbations of the real and imaginary parts of the refractive index. As it is not necessary to dope the waveguide core of a d.c. Kerr phase shifter, there is no amplitude chirp due to the d.c. Kerr effect. Besides, plasma-dispersion-based shifters rely on a large-capacitance p-n junction to maximize the electro-optic response, limiting the bandwidth²⁴, but the d.c. Kerr effect is based on a low-capacitance p-i-n junction. These properties enable low-loss, chirp-free and high-bandwidth modulators in a MZI configuration. Therefore, complex modulation formats, coherent communications, radiofrequency (RF) links and electro-optic analog-to-digital conversion can be realized with d.c. Kerr-effect-based MZI modulators without signal equalization.

EFISHG design

Another common application of materials exhibiting $\chi^{(2)}$ is SHG. Unlike the inherently phase-matched d.c. Kerr effect, EFISHG requires phase-matching of the pump and frequency-doubled signal. For EFISHG, the x -polarized pump and signal modes (e_{ω}^x , $e_{2\omega}^x$) in a silicon ridge waveguide were both chosen to be fundamental TE modes (Fig. 2a,b).

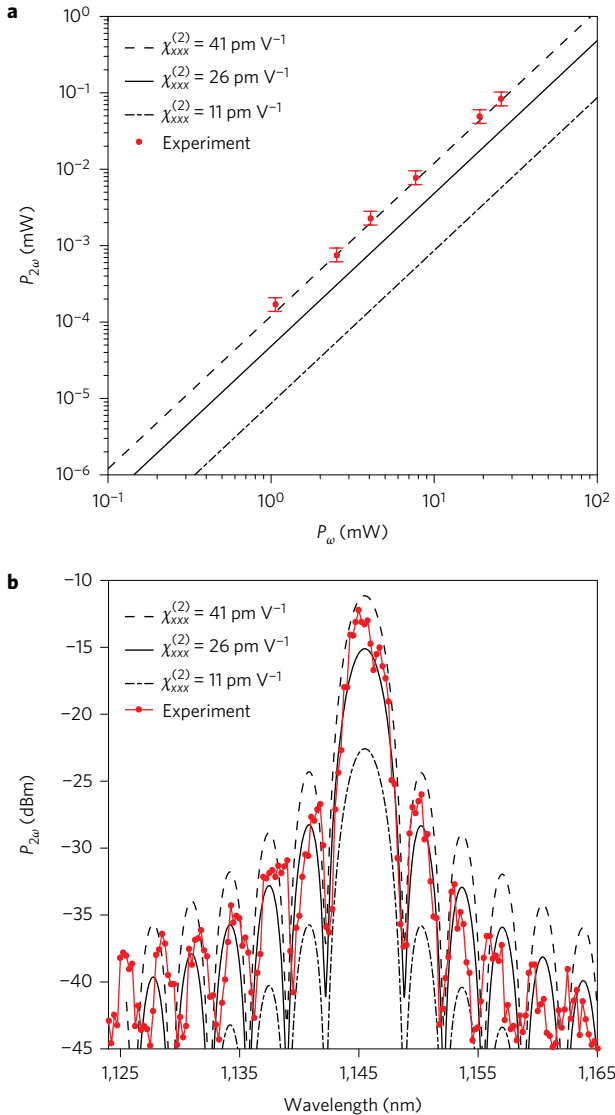


Figure 3 | Analytical and experimental SHG. **a,b**, Analytically calculated on-chip SHG curves for estimated second-order susceptibilities from refs 27–33 are plotted as a function of pump power (**a**) and wavelength (**b**). Measurement data are overlaid, showing an effective second-order nonlinearity of $\bar{\chi}_{xxx}^{(2)} = 41 \text{ pm V}^{-1}$ when the p–i–n junction is reverse-biased at 21 V ($E_{dc}^x \approx 25 \text{ V } \mu\text{m}^{-1}$). The c.w. pump power is $P_\omega = 25 \text{ mW}$ in **b**.

Fundamental modes achieve maximal confinement in the silicon core, and a large overlap between pump and second-harmonic signals. In this case, the induced second-order nonlinear susceptibility is related to the third-order nonlinear susceptibility by equation (1): $\chi_{xxx}^{(2)} = 3\chi_{xxxx}^{(3)} E_{dc}^x$ (ref. 19). In this case, we chose signal and pump wavelengths equal to $\lambda_{2\omega} \approx 1.145 \text{ } \mu\text{m}$ and $\lambda_\omega \approx 2.29 \text{ } \mu\text{m}$. The signal wavelength was selected to be within the transparent silicon region to minimize absorption. We used the model in ref. 27 and the third-order nonlinearities in refs 4 and 27–33 to estimate the tensor element to be $\chi_{xxxx}^{(3)} = (6 \pm 3.5) \times 10^{-19} \text{ m}^2 \text{ V}^{-2}$ at $\lambda_\omega \approx 2.29 \text{ } \mu\text{m}$. This uncertainty arises from large differences in the reported $\chi^{(3)}$ of silicon around $\lambda_\omega \approx 2.29 \text{ } \mu\text{m}$ (refs 27–33). As a consequence, the bulk second-order nonlinearity within the silicon waveguide can be as large as $\chi_{xxx}^{(2)} = 3\chi_{xxxx}^{(3)} E_{dc}^x = 72 \pm 42 \text{ pm V}^{-1}$ for an applied field that is equal to the silicon breakdown field, $E_{dc}^x = 40 \text{ V } \mu\text{m}^{-1}$. The effective second-order nonlinear susceptibility, $\bar{\chi}_{xxx}^{(2)}$, that acts upon the pump and signal modes, is determined using the overlap integral over the intrinsic silicon area, v_1 , and the waveguide area, v_0 ,

$\bar{\chi}_{xxx}^{(2)} = 3\chi_{xxxx}^{(3)} \sqrt{v_1} \int_{v_0} e_{2\omega}^x e_\omega^x E_{dc}^x dV$. The core of the silicon waveguide was chosen to be 800 nm wide to maximize the overlap integral between the fundamental TE pump and signal modes while minimizing the required electrical voltage for generating large electric fields (Fig. 2c). We simulated the electric field within the silicon core waveguide using the Sentaurus software suite from Synopsys. When a reverse bias of 21 V was applied to the junction, the electric field was quite uniform inside the silicon core with $E_{dc}^x = 25 \text{ V } \mu\text{m}^{-1}$, and the effective second-order nonlinearity was simulated to be $\bar{\chi}_{xxx}^{(2)} = 26 \pm 15 \text{ pm V}^{-1}$.

Although a large second-order nonlinearity can be induced in silicon, the pump and signal propagation constants (k_ω , $k_{2\omega}$) are required to be phase-matched for efficient SHG, $2k_\omega - k_{2\omega} = 0$. This is not the case for the fundamental TE optical modes due to waveguide and material dispersion, $k_\omega = 6.132 \text{ } \mu\text{m}^{-1}$ and $k_{2\omega} = 16.627 \text{ } \mu\text{m}^{-1}$ at $\lambda_\omega \approx 2.29 \text{ } \mu\text{m}$ and $\lambda_{2\omega} \approx 1.145 \text{ } \mu\text{m}$ (see Methods, ‘Eigenmode simulations’). Therefore, the pump and signal should be coupled only when both are in phase, and decoupled when both are out of phase. This condition is referred to as quasi-phase-matching. A spatially periodic electric field along the waveguide is required to quasi-phase-match pump and signal modes in silicon. We thus added lateral p–i–n junctions with a period of $\Lambda = 1.44 \text{ } \mu\text{m}$ to realize the periodic electric field (Fig. 2d). The period was selected to correspond to twice the coherence length for first-order quasi-phase matching^{19,34}: $2k_\omega^{\text{TE}_{11}} - k_{2\omega}^{\text{TE}_{11}} + (2\pi/\Lambda) = 0$. The generated second-harmonic power $P_{2\omega}$ for a quasi-phase-matched nonlinear medium was derived using nonlinear coupled mode theory and the undepleted-pump approximation in ref. 19:

$$P_{2\omega} = \frac{8\bar{\chi}_{xxx}^{(2)} L_{\text{qpm}}^2 P_\omega^2}{\epsilon_0 n_\omega^2 n_{2\omega} c \lambda_\omega^2 A} \exp[-(2\alpha_\omega + \alpha_{2\omega})L/2] \times \frac{\sin^2[\Delta k L_{\text{qpm}}/2] + \sinh^2[(2\alpha_\omega - \alpha_{2\omega})L/4]}{(\Delta k L_{\text{qpm}}/2)^2 + [(2\alpha_\omega - \alpha_{2\omega})L/4]^2} \quad (2)$$

where $n_\omega = 2.245$ and $n_{2\omega} = 3.043$ are the effective refractive indices at the pump and signal wavelengths, $\alpha_\omega = 3.6 \text{ cm}^{-1}$ (15.6 dB cm^{-1}) and $\alpha_{2\omega} = 0.2 \text{ cm}^{-1}$ (0.9 dB cm^{-1}) are the simulated optical power loss coefficients at pump and signal wavelengths, P_ω is the pump power, $A = 0.0915 \text{ } \mu\text{m}^2$ is the modal area, $L = 1 \text{ mm}$ and $L_{\text{qpm}} = 0.5 \text{ mm}$ are the nonlinear waveguide and quasi-phase-matched section lengths, and $\Delta k = k_{2\omega}^{\text{TE}_{11}} - 2k_\omega^{\text{TE}_{11}} - 2\pi/\Lambda = 2\pi n_{2\omega}/\lambda_{2\omega} - 4\pi n_\omega/\lambda_\omega - 2\pi/\Lambda$ is the phase mismatch between the pump and second-harmonic signal, including the quasi-phase-matched period. The pump power dependence of the SHG was calculated using equation (2) (Fig. 3a). The SHG efficiency was estimated to be within $0.9 \leq P_{2\omega}/P_\omega^2 \leq 12\% \text{ W}^{-1}$. The spectral response of SHG at $P_\omega = 25 \text{ mW}$ was also calculated using equation (2) (Fig. 3b). The spectral bandwidth of the main lobe was 6.5 nm. This efficiency can be achieved if the duty cycle is fixed within each period (see Methods, ‘Duty cycle errors’). Furthermore, when the waveguide width and the spatial period are altered in different waveguides, the quasi-phase-matched pump wavelength was designed to be within $\lambda_\omega = 2\lambda_{2\omega} = 2.15 \text{ } \mu\text{m}$ and $\lambda_\omega = 2\lambda_{2\omega} = 2.42 \text{ } \mu\text{m}$. The pump depletion is calculated to be effective beyond 1 W pump power inside silicon¹⁹ and was negligible in this power range ($P_\omega < 100 \text{ mW}$).

EFISHG results and discussion

The designed second-harmonic generators were fabricated on a 300 mm SOI wafer (Fig. 4a,b). The p–i–n junctions within the waveguide were reverse-biased from -0.7 to 21 V. When the devices were reverse-biased further than 21 V, the response was not stable due to leakage current. SHG was not observed when the junction was forward-biased ($V_{dc} < -0.5 \text{ V}$) or the spatial period did not provide the proper quasi-phase matching for the pump and signal wavelengths. This behaviour indicates negligible background SHG

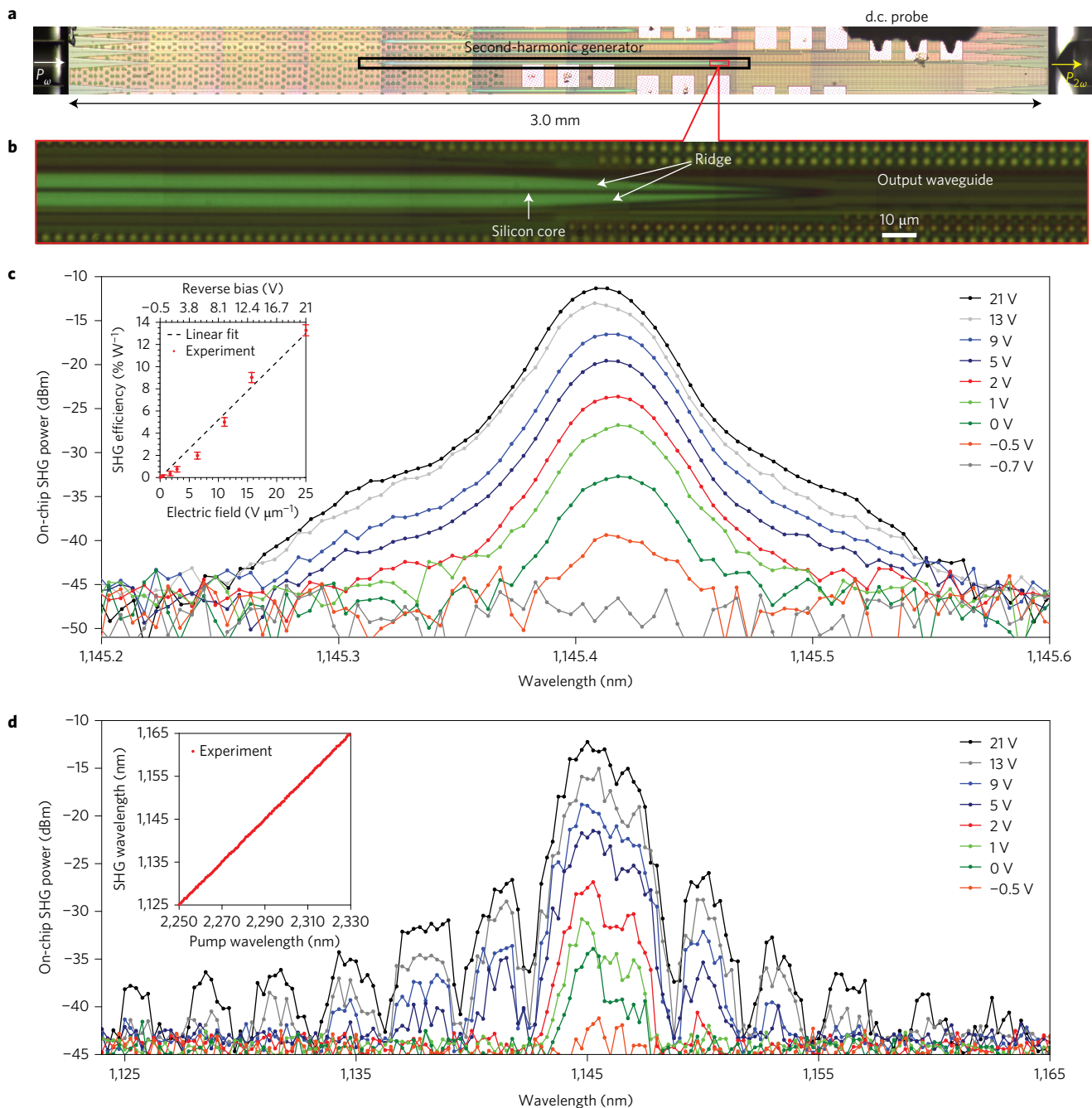


Figure 4 | Voltage and power dependence of the SHG. **a,b**, Optical micrograph images of the integrated SHG shown with coupled single-mode fibres (left, SMF-2000; right, SMF-28). The d.c. ground-signal-ground probe is shown in **a**, and the silicon ridge waveguide in **b**. The close-up section is highlighted in the top image with a red rectangle. **c**, On-chip generated c.w. second-harmonic power measured with an OSA as a function of applied reverse bias. The c.w. pump was lasing at $\lambda \approx 2.29 \mu\text{m}$ and power was $P_{\omega} = 25 \text{ mW}$. Inset: summary of the measured SHG efficiency $P_{2\omega}/P_{\omega}^2$ as a function of applied reverse bias and electric field. **d**, Dependence of SHG power measured with an OSA as a function of swept wavelength and applied reverse bias. Inset: measured linearity of the pump and SHG wavelength dependence by OSAs, showing true harmonic generation.

from other contributions. We recorded the second-harmonic signal as a function of the applied d.c. bias, as shown in Fig. 4c (see Methods, ‘EFISHG measurements’). The measurement uncertainty due to fibre-to-chip coupling was $\pm 0.5 \text{ dB}$. Linear scaling of SHG efficiency as a function of the electric field was also recorded (Fig. 4c, inset). The maximum SHG efficiency was measured to be $P_{2\omega}/P_{\omega}^2 = 13 \pm 0.5\% \text{ W}^{-1}$ at a pump wavelength of $\lambda_{\omega} \approx 2.29 \mu\text{m}$ and a reverse bias of $V_{\text{dc}} = 21 \text{ V}$. The uncertainty of the SHG efficiency originated from the fluctuations of the optical power during measurements. The reverse-bias current passing through

the p-i-n junction was below $0.1 \mu\text{A}$ at $V_{\text{dc}} = 21 \text{ V}$, and electric fields were below the breakdown field of silicon. Overlaying the measurement results with the simulations in Fig. 3a, we determined the effective field-induced second-order nonlinear susceptibility $\bar{\chi}^2$ to be $41 \pm 1.5 \text{ pm V}^{-1}$. These results matched well the upper limit of the reported third-order nonlinear susceptibilities^{4,27–33}. The SHG power was also measured with external optical spectrum analysers (OSAs) as a function of reverse-bias voltage and signal and pump wavelengths, as shown in the inset to Fig. 4d. In this case, the measurement uncertainty due to fibre-to-chip coupling was

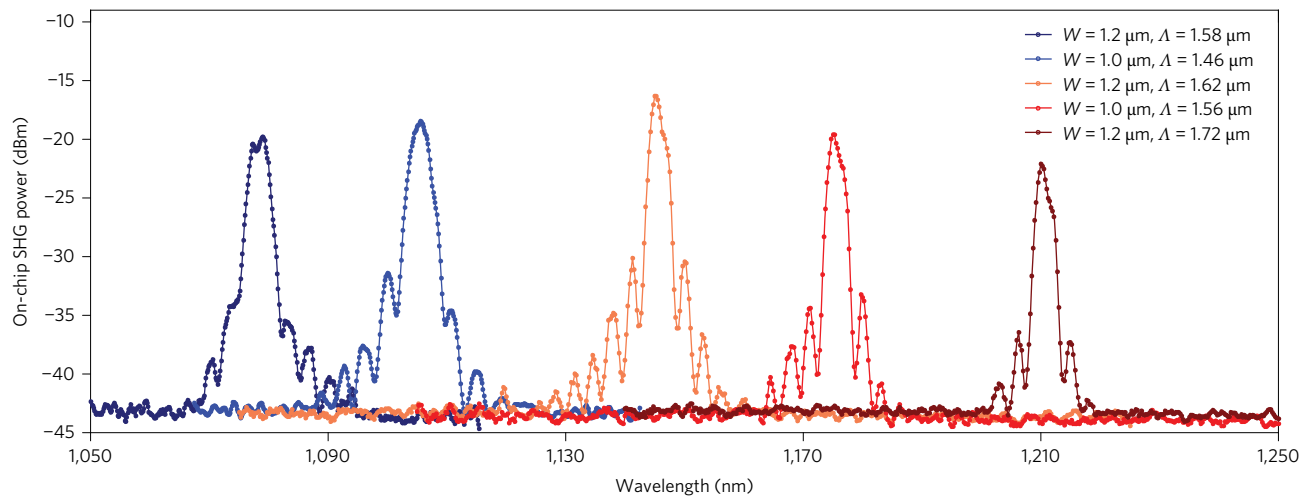


Figure 5 | SHG at multiple wavelengths. SHG of separate waveguides with different quasi-phase-matching periods and input wavelengths. The c.w. pump power is $P_{\omega} = 19$ mW and $E_{dc}^x \approx 25$ V μm^{-1} at all wavelengths.

± 0.9 dB. The expected sinc²-like response and doubling of pump frequency at the second-harmonic frequency are illustrated in Fig. 4d. We note that the spectral sidebands of the sinc²-like response increased slightly faster than the main peak for an increasing d.c. field, providing additional insight into the ultimate limitations of field-induced second-order nonlinear wave mixing efficiency in a CMOS-compatible platform. The spectral response at a reverse bias of $V_{dc} = 21$ V is overlaid with the simulations in Fig. 3b for comparison with theory. Furthermore, when we tested the waveguides with different widths and spatial periods, we observed SHG at multiple wavelengths spanning from $\lambda_{\omega} = 2\lambda_{2\omega} = 2.16$ μm to $\lambda_{\omega} = 2\lambda_{2\omega} = 2.42$ μm , showing good agreement with the simulated quasi-phase-matched pump wavelengths (Fig. 5). The measurement uncertainty due to fibre-to-chip coupling was again ± 0.9 dB. The performances of the integrated second-harmonic generators considered here (and those of alternative platforms) are provided in Table 1, showing that the conversion efficiency of EFISHG in silicon is a major step towards a CMOS-compatible efficient SHG. Such second-harmonic generators can enable many potential applications, one of which is the extraction and locking of the carrier-envelope frequency offset for an octave-spanning supercontinuum signal that spans from ~ 1.08 to ~ 2.42 μm (ref. 35).

Conclusions

We have demonstrated electric-field-induced second-order nonlinear susceptibility in silicon waveguides using CMOS-compatible fabrication methods. The origin of this second-order nonlinearity is the large third-order nonlinear susceptibility of silicon combined

with large electric fields generated within reverse-biased p–i–n junctions, breaking the crystalline symmetry of silicon. The d.c. Kerr effect in silicon is used as an optical phase shifter in multiple MZIs, demonstrating a $V_{\pi}L$ as low as 2.8 V cm. We expect this technology to allow for non-distorted translation of electronic-to-photon signals, leading to linear, analog transmitters for RF, microwave photonics and photonic digital-to-analog converters with minimum signal processing and compensation. These modulators could be ideal candidates to replace plasma-dispersion-based modulators in data centres, high-performance computers and telecom devices. We also obtained a second-order nonlinear susceptibility with a quasi-phase-matched EFISHG device, measuring a conversion efficiency of $P_{2\omega}/P_{\omega}^2 = 13 \pm 0.5\%$ W^{-1} at $\lambda_{\omega} = 2\lambda_{2\omega} = 2.29$ μm that corresponds to an effective field-induced $\tilde{\chi}^2$ of 41 ± 1.5 pm^{-1} . Changing the waveguide width and the spatial period, SHG was also measured at wavelengths ranging from $\lambda_{\omega} = 2.16$ μm to $\lambda_{\omega} = 2.42$ μm . Future work will look into sum/difference frequency generation for applications such as lasers at telecom or mid-infrared wavelengths and terahertz generation.

Methods

Methods and any associated references are available in the [online version of the paper](#).

Received 14 March 2016; accepted 17 January 2017; published online 20 February 2017

References

- Boyd, R. W. *Nonlinear Optics* 2nd edn (Academic, 2002).
- Corcoran, B. *et al.* Green light emission in silicon through slow-light enhanced third-harmonic generation in photonic-crystal waveguides. *Nat. Photon.* **3**, 206–210 (2009).
- Sederberg, S. & Elezabi, A. Y. Coherent visible-light-generation enhancement in silicon-based nanoplasmonic waveguides via third-harmonic generation. *Phys. Rev. Lett.* **144**, 227401 (2015).
- Dulkeith, E., Vlasov, Y. A., Chen, X., Panoiu, N. C. & Osgood, R. M. Self-phase-modulation in submicron silicon-on-insulator photonic wires. *Opt. Express* **14**, 5524–5534 (2006).
- Lin, Q., Painter, O. J. & Agrawal, G. P. Nonlinear optical phenomena in silicon waveguides: modeling and applications. *Opt. Express* **15**, 16604–16644 (2007).
- Moss, D. J., van Driel, H. M. & Sipe, J. E. Dispersion in the anisotropy of optical third-harmonic generation in silicon. *Opt. Lett.* **14**, 57–59 (1989).
- Cundiff, S. T. & Ye, J. *Femtosecond Optical Frequency Comb: Principle, Operation and Applications* (Springer Science, 2005).
- Cazzanelli, M. *et al.* Second-harmonic generation in silicon waveguides strained by silicon nitride. *Nat. Mater.* **11**, 148–154 (2012).
- Ning, T. *et al.* Strong second-harmonic generation in silicon nitride films. *Appl. Phys. Lett.* **100**, 161902 (2012).

Table 1 | Comparison of performance for integrated SHG and other platforms.

Media	Type	$\chi^{(2)}$ (pm V^{-1})*	Length (μm) [†]	$\eta = P_{2\omega}/P_{\omega}^2$ (% W^{-1}) [‡]	Ref.
Si	Strained	40	2×10^3	0.00001	8
SiN	Resonant	0.04	$2\pi \times 116$	0.1	10
LiNbO ₃	QPM	69	1×10^4	204	11
GaAs	Resonant	–	$2\pi \times 2.6$	5.2	12
GaN	Resonant	16	$2\pi \times 40$	0.02	13
Si	QPM EFISHG	41	1×10^3	13	This work

The table shows that the device performance reported in this work is comparable with that achieved in non-centro-symmetric media. *Second-order nonlinear susceptibility of the material; [†]length of the integrated SHG structure; [‡]measured SHG efficiency, defined here as the ratio of SHG power to the power in the fundamental squared. QPM, quasi-phase-matched.

10. Levy, J. S., Foster, M. A., Gaeta, A. L. & Lipson, M. Harmonic generation in silicon nitride ring resonators. *Opt. Express* **19**, 11415–11421 (2011).
11. Bortz, M. L. *et al.* Noncritical quasi-phase-matched second harmonic generation in an annealed proton-exchanged LiNbO₃ waveguide. *IEEE J. Quantum Electron.* **30**, 2953–2960 (1994).
12. Kuo, P. S., Bravo-Abad, J. & Solomon, G. S. Second-harmonic generation using 4-quasi-phase-matching in a GaAs whispering-gallery-mode microcavity. *Nat. Commun.* **5**, 3109 (2014).
13. Xiong, C. *et al.* Integrated GaN photonic circuits on silicon (100) for second harmonic generation. *Opt. Express* **19**, 10462–10470 (2011).
14. Maker, P. D. & Terhune, R. W. Study of optical effects due to an induced polarization third order in the electric field strength. *Phys. Rev.* **137**, A801–A818 (1965).
15. Lüpke, G. Characterization of semiconductor interfaces by second-harmonic generation. *Surf. Sci. Rep.* **35**, 75–161 (1999).
16. Baehr-Jones, T. *et al.* Optical modulation and detection in slotted silicon waveguides. *Opt. Express* **13**, 5216–5226 (2005).
17. Hochberg, M. *et al.* Towards a millivolt optical modulator with nano-slot waveguides. *Opt. Express* **15**, 8401–8410 (2007).
18. Schriever, C. *et al.* Second-order optical nonlinearity in silicon waveguides: inhomogeneous stress and interfaces. *Adv. Opt. Mater.* **3**, 129–136 (2015).
19. Sutherland, R. L. *Handbook of Nonlinear Optics* (CRC, 2003).
20. Soref, R. A. & Bennett, B. R. Electrooptical effects in silicon. *IEEE J. Quantum Electron.* **23**, 123–129 (1987).
21. Kashyap, R. Phase-matched periodic electric-field-induced second-harmonic generation in optical fibers. *J. Opt. Soc. Am. B* **6**, 313–328 (1989).
22. Qasymeh, M., Cada, M. & Ponomarenko, S. A. Quadratic electro-optic Kerr effect: applications to photonic devices. *IEEE J. Quantum Electron.* **44**, 740–746 (2008).
23. Popović, M. in *Integrated Photonics Research* Vol. 91 (ed. Sawchuk, A.) paper ITuD4 (OSA Trends in Optics and Photonics, Optical Society of America, 2003).
24. Timurdogan, E. *et al.* An ultralow power athermal silicon modulator. *Nat. Commun.* **5**, 4008 (2014).
25. Azadeh, S. S., Merget, F., Nezhad, M. P. & Witzens, J. On the measurement of the Pockels effect in strained silicon. *Opt. Lett.* **40**, 1877–1880 (2015).
26. Sharma, R. *et al.* Characterizing the effects of free carriers in fully etched, dielectric-clad silicon waveguides. *Appl. Phys. Lett.* **106**, 241104 (2015).
27. Hon, N. K., Soref, R. & Jalali, B. The third-order nonlinear optical coefficients of Si, Ge, and Si_{1-x}Ge_x in the midwave and longwave infrared. *J. Appl. Phys.* **110**, 011301 (2011).
28. Bristow, A. D., Rotenberg, N. & van Driel, H. M. Two-photon absorption and Kerr coefficients of silicon for 850–2200 nm. *Appl. Phys. Lett.* **90**, 191104 (2007).
29. Pearl, S., Rotenberg, N. & van Driel, H. M. Three photon absorption in silicon for 2300–3300 nm. *Appl. Phys. Lett.* **93**, 131102 (2008).
30. Lin, Q. *et al.* Dispersion of silicon nonlinearities in the near infrared region. *Appl. Phys. Lett.* **91**, 021111 (2007).
31. Wang, T. *et al.* Multi-photon absorption and third-order nonlinearity in silicon at mid-infrared wavelengths. *Opt. Express* **21**, 32192–32198 (2013).
32. Gholami, F. *et al.* Third-order nonlinearity in silicon beyond 2350 nm. *Appl. Phys. Lett.* **99**, 081102 (2011).
33. Dinu, M., Quochi, F. & Garcia, H. Third-order nonlinearities in silicon at telecom wavelengths. *Appl. Phys. Lett.* **82**, 2954–2956 (2003).
34. Szilagyi, A., Hordvik, A. & Schlossberg, H. A quasi-phase-matching technique for efficient optical mixing and frequency doubling. *J. Appl. Phys.* **47**, 2025–2032 (1976).
35. Telle, H. R. *et al.* Carrier-envelope offset phase control: a novel concept for absolute optical frequency measurement and ultrashort pulse generation. *Appl. Phys. B* **69**, 327–332 (1999).

Acknowledgements

This work was supported by the Defense Advanced Research Projects Agency (DARPA) Microsystems Technology Office (MTO) E-PHI (HR0011-12-2-0007) and DODOS (HR0011-15-C-0056) projects. The authors thank programme managers J. Conway and R. Lutwak for support.

Author contributions

E.T. and M.R.W. conceived the idea for the project. E.T. simulated and designed nonlinear silicon waveguides, laid out the mask, conducted experiments on second-harmonic generators and analysed the results. E.T. and C.V.P. designed the d.c. Kerr MZIs, laid out the mask and analysed the results. C.V.P., M.J.B. and E.T. conducted experiments on d.c. Kerr MZIs. All authors wrote and edited the manuscript. M.R.W. supervised the project.

Additional information

Reprints and permissions information is available online at www.nature.com/reprints. Correspondence and requests for materials should be addressed to E.T.

Competing financial interests

The authors declare no competing financial interests.

Methods

Device fabrication. The silicon ridge waveguide with an integrated lateral p–i–n junction was fabricated in a 300-mm-diameter wafer CMOS foundry using SOI wafers with a 225 nm top silicon layer and a 2 μm buried oxide (BOX) layer for optical isolation. The SOI was fully etched to form the waveguides. It was followed by a partial silicon etch to form the ridge waveguides. The etch depth was 110 nm. An oxidation step was used to passivate the sidewalls, which reduced the full waveguide thickness to 220 nm and the ridge thickness to 100 nm. The p–i–n junction was formed by arsenic (As) and boron difluoride (BF_2) implants with target doping concentrations of 10^{18} cm^{-3} . The n^+ - and p^+ -doped contact regions are formed by phosphorus (P) and BF_2 implants with target concentrations of $\sim 1 \times 10^{20} \text{ cm}^{-3}$. The tungsten vias were contacted to highly doped regions by self-aligned silicidation. Two copper routing layers were used to contact on-chip ground–signal–ground (GSG) d.c. probing pads ($60 \times 60 \mu\text{m}^2$) at a 100 μm pitch.

Process and electrical simulations. Process simulations for silicon ridge waveguides were performed following the device fabrication steps in Synopsys' Sentaurus Process to form p–i–n junctions within these waveguides. The waveguides were then d.c. biased in a Sentaurus Device (Synopsys). The carrier distributions and depletion widths were extracted as a function of applied voltage bias.

Eigenmode simulations. The silicon and SiO_2 refractive indices for pump and signal wavelengths were determined using the fit parameters to Sellmeier's equation in ref. 36. The carrier distribution within the silicon ridge waveguide was simulated using the Sentaurus Process and Device. The carrier distribution was converted to an electro-refractive index distribution using the fit parameters for the plasma-dispersion effect in ref. 24. These fit parameters were extracted at $\lambda_{\text{er}} \approx 1.55 \mu\text{m}$. The electro-refractive index distributions at pump and signal wavelength were scaled by $(\lambda_{\omega}/\lambda_{\text{er}})^2$ and $(\lambda_{2\omega}/\lambda_{\text{er}})^2$, following the plasma-dispersion relation in ref. 20. The refractive indices and electro-refractive index distributions at pump and signal wavelengths were combined, respectively. The mode profiles and complex propagation constants for the resulting index distributions were simulated using a finite-difference modesolver²³. The loss coefficients at pump and signal wavelengths were extracted from the imaginary part of the complex propagation constants.

In equation (1), the d.c. Kerr relative permittivity is expressed as $\Delta\epsilon_{\text{dc Kerr}} = 12\chi_{\text{xxxx}}^{(3)} E_{\text{dc}}^2$, where the electric field is $E_{\text{dc}}^x = V_{\text{dc}}/W_1$ and V_{dc} is the reverse bias. Assuming a small perturbation to the refractive index, the index perturbation was approximated with $\Delta n_{\text{dc Kerr}} = \Delta\epsilon_{\text{dc Kerr}}/(2\sqrt{\epsilon_{\text{Si}}})$ (ref. 24). The overlap integral between the intrinsic region and the optical mode was used to determine the effective d.c. Kerr index perturbation, $\Delta n_{\text{eff}} = \int_V \Delta n_{\text{dc Kerr}} e_{\omega}^x e_{\omega}^x dV$ where the optical mode (e_{ω}^x) was normalized using $\int_V e_{\omega}^x e_{\omega}^x dV = 1$.

Direct-current Kerr measurements. For the d.c. Kerr phase shifters, the optical path difference between the MZ arms was minimized with a silicon heater in one of

the MZ arms. The other arm of the MZI was also doped to minimize the loss difference between the arms. A c.w. laser at $\lambda \approx 1,580 \text{ nm}$ was coupled through a single-mode fibre (SMF-28) to an inverse silicon taper. The linearly polarized output of the SMF-28 and the fundamental TE mode of the on-chip waveguide were aligned using a fibre polarization controller. Another SMF-28 fibre was used to collect the output light. The insertion losses due to the fibre couplers were subtracted before fitting the cross and bar ports.

EFISHG measurements. For the EFISHG devices, a near-infrared c.w. tunable pump laser was free-space-coupled to one end of a single-mode fibre (SMF-2000) and the other end of the fibre was cleaved. The cleaved fibre end was used to couple the pump laser to an on-chip inverse silicon taper. A polarization controller was used to align the linearly polarized output of the SMF-2000 and the fundamental TE mode of the on-chip waveguide. The on-chip pump and harmonic powers were calibrated by measuring fibre-to-chip coupling losses (12 dB and 6 dB for pump and signal wavelengths) and waveguide losses ($\alpha_{\omega} = 3.3 \text{ cm}^{-1}$ (14.3 dB cm^{-1}) and $\alpha_{2\omega} = 0.3 \text{ cm}^{-1}$ (1.3 dB cm^{-1})) using waveguides with varying lengths. The waveguide losses were in agreement with the simulated numbers. The maximum on-chip pump power around $\lambda_{\omega} \approx 2.29 \mu\text{m}$ was measured to be $P_{\omega} = 25 \text{ mW}$, limited by the coupling losses and pump laser. The second-harmonic signal was collected using a lensed single-mode fibre (SMF-28) and the wavelengths of both pump and second-harmonic signals were measured using external OSAs.

Duty cycle errors. Lithography can lead to errors in duty cycle³⁷. The expected conversion efficiency as a function of duty cycle errors, η , normalized to the ideal η_0 , is derived to be $\eta/\eta_0 = e^{-(\sqrt{2}\pi\sigma/\Lambda)^2}$, where σ is the root-mean-square (r.m.s.) error in the duty cycle. An r.m.s. duty cycle error of $\sigma/\Lambda = 1/5.4$ halves the conversion efficiency but the expected mask alignment error is $\sigma/\Lambda < 1/20$ in the silicon photonics platform, which corresponds to less than a 5% reduction in conversion efficiency.

Data availability. The data that support the plots within this paper and other findings of this study are available from the corresponding author upon reasonable request.

References

- Avrutsky, I. & Soref, R. Phase-matched sum frequency generation in strained silicon waveguides using their second-order nonlinear optical susceptibility. *Opt. Express* **19**, 21707–21716 (2011).
- Fejer, M. M., Magel, G. A., Jundt, D. H. & Byer, R. L. Quasi-phase-matched second harmonic generation: tuning and tolerances. *IEEE J. Quantum Electron.* **28**, 2631–2654 (1992).